Monthly Notices of the ROYAL ASTRONOMICAL SOCIETY

MNRAS **499,** 4863–4875 (2020) doi:10.1093/mnras/staa3109
Advance Access publication 2020 October 10

Predicting accreted satellite galaxy masses and accretion redshifts based on globular cluster orbits in the E-MOSAICS simulations

Joel L. Pfeffer [1]★ Sebastian Trujillo-Gomez [2] J. M. D. Kruijssen [2] Robert A. Crain [1] Meghan E. Hughes [1] Marta Reina-Campos [2] and Nate Bastian[1]

[1]*Astrophysics Research Institute, Liverpool John Moores University, 146 Brownlow Hill, Liverpool L3 5RF, UK*
[2]*Astronomisches Rechen-Institut, Zentrum für Astronomie der Universität Heidelberg, Mönchhofstraße 12-14, D-69120 Heidelberg, Germany*

Accepted 2020 September 21. Received 2020 July 31; in original form 2020 March 1

ABSTRACT

The ages and metallicities of globular clusters (GCs) are known to be powerful tracers of the properties of their progenitor galaxies, enabling their use in determining the merger histories of galaxies. However, while useful in separating GCs into individual accretion events, the orbits of GC groups themselves have received less attention as probes of their progenitor galaxy properties. In this work, we use simulations of galaxies and their GC systems from the MOdelling Star cluster population Assembly In Cosmological Simulations within EAGLE project to explore how the present-day orbital properties of GCs are related to the properties of their progenitor galaxies. We find that the orbits of GCs deposited by accretion events are sensitive to the mass and merger redshift of the satellite galaxy. Earlier mergers and larger galaxy masses deposit GCs at smaller median apocentres and lower total orbital energy. The orbital properties of accreted groups of GCs can therefore be used to infer the properties of their progenitor galaxy, though there exists a degeneracy between galaxy mass and accretion time. Combining GC orbits with other tracers (GC ages, metallicities) will help to break the galaxy mass/accretion time degeneracy, enabling stronger constraints on the properties of their progenitor galaxy. *In situ* GCs generally orbit at lower energies (small apocentres) than accreted GCs, however they exhibit a large tail to high energies and even retrograde orbits (relative to the present-day disc), showing significant overlap with accreted GCs. Applying the results to Milky Way GCs groups suggests a merger redshift $z \sim 1.5$ for the *Gaia* Sausage/Enceladus and $z > 2$ for the 'low-energy'/*Kraken* group, adding further evidence that the Milky Way had two significant mergers in its past.

Key words: methods: numerical – stars: formation – globular clusters: general – galaxies: evolution – galaxies: formation – galaxies: star clusters: general.

1 INTRODUCTION

A major objective in astrophysics is to understand the formation and assembly of the Milky Way. This has been undertaken from many different angles, combining stellar chemical compositions and ages with their spatial and kinematic properties (e.g. Eggen, Lynden-Bell & Sandage 1962; Searle & Zinn 1978; Chiba & Beers 2000; Carollo et al. 2007). These works have since confirmed that the Galaxy formed in a continuous hierarchical process (White & Rees 1978; Blumenthal et al. 1984) through a combination of *in situ* star formation from accreted and reprocessed gas, and the accretion and merging of satellites which experienced their own chemical evolution (see reviews by Majewski 1993; Freeman & Bland-Hawthorn 2002; Helmi 2008).

Despite ongoing debates about their origin (for recent reviews, see Kruijssen 2014; Forbes et al. 2018), globular clusters (GCs) also have a similarly long history of being used as probes of the galaxy formation and assembly process, particularly in the Milky Way (e.g. Searle & Zinn 1978; Dinescu, Girard & van Altena 1999; Brodie & Strader 2006). The properties of Milky Way GCs, such as their orbits (e.g. Lin & Richer 1992; Dinescu et al. 1999), metallicities and ages (e.g. Marín-Franch et al. 2009; Forbes & Bridges 2010; Leaman, VandenBerg & Mendel 2013; Kruijssen et al. 2019b), horizontal branch morphology (e.g. van den Bergh 1993; Zinn 1993; Mackey & Gilmore 2004), and chemical abundances (e.g. Brown, Wallerstein & Zucker 1997; Pritzl, Venn & Irwin 2005; Horta et al. 2020), have been used to distinguish their origin (accretion or *in situ* formation) and derive the properties of their progenitor galaxies which have long since been accreted. The orbital properties of GCs, in particular, hold great promise in separating the GCs of individual accretion events if their orbital properties remain clustered (e.g. in integrals of motion).

The release of proper motions from the *Gaia* mission (Gaia Collaboration 2016, 2018), in particular the second data release, has seen a major advance in deriving the orbits of field stars and GCs and generated a large number of works on the assembly history of the Milky Way and the origin of its GC population (e.g. Belokurov et al. 2018, 2020; Deason et al. 2018; Haywood et al. 2018; Helmi et al. 2018; Myeong et al. 2018a,c,b,d, 2019; Deason, Belokurov & Sanders 2019; Di Matteo et al. 2019; Iorio & Belokurov 2019; Koppelman et al. 2019a,b; Mackereth et al. 2019; Massari,

★ E-mail: j.l.pfeffer@ljmu.ac.uk

Koppelman & Helmi 2019; Necib et al. 2019, 2020; Vasiliev 2019). A major outcome of these works is that the outer stellar halo (>10 kpc) of the Milky Way appears to be dominated by the debris from a single merged satellite, the *Gaia* Sausage/Enceladus (G-E), which was accreted ∼9–10 Gyr ago (Belokurov et al. 2018; Haywood et al. 2018; Helmi et al. 2018; Myeong et al. 2018d, 2019; Bignone, Helmi & Tissera 2019; Conroy et al. 2019; Mackereth et al. 2019; Kruijssen et al. 2020). Along with G-E, the analysis of *Gaia* DR2 data has resulted in the discovery of a number of less massive substructures and the characterization of their progenitor galaxies (e.g. Sequoia, Myeong et al. 2019; Thamnos, Koppelman et al. 2019b) and further constrained the progenitor properties of already known substructures (e.g. Helmi streams, Helmi et al. 1999; Koppelman et al. 2019a).

Massari et al. (2019) also found evidence for a population of GCs in the Milky Way at low energies (the L-E group) which do not appear to have formed *in situ* in the Galaxy (the GCs have ages and metallicities consistent with the 'accreted' or 'satellite' branch[1]), and are not connected to previously known merger events. This GC population is plausibly consistent with the proposed *Kraken* (Kruijssen et al. 2019b) accretion event, which was predicted based on number of GCs in the 'satellite' branch of the Milky Way GC age–metallicity distribution (see also Forbes 2020; Kruijssen et al. 2020).

In this work, we use the hydrodynamical, cosmological simulations of galaxy formation including GC formation and evolution from the MOdelling Star cluster population Assembly In Cosmological Simulations within EAGLE project (E-MOSAICS; Pfeffer et al. 2018; Kruijssen et al. 2019a) to investigate the orbits of accreted and *in situ* GCs. The E-MOSAICS simulations have previously been used to investigate the origin and evolution of GCs (Pfeffer et al. 2018; Reina-Campos et al. 2018, 2019; Usher et al. 2018; Hughes et al. 2020; Keller et al. 2020), the use of GCs to trace the formation and assembly of galaxies (Kruijssen et al. 2019a,b; Hughes et al. 2019; Trujillo-Gomez et al. 2020) and the properties of young clusters at high and low redshifts (Pfeffer et al. 2019a,b). This work explores how the orbital properties of accreted GCs can be related to their progenitor galaxy properties (mass and accretion time). In this paper, we aim to test which types of galaxy accretion events could place GCs on orbits similar to the G-E and L-E groups, and test whether the latter is consistent with the proposed Kraken accretion event. Additionally, we compare the orbital properties of GCs formed *in situ* within the main progenitor galaxies and investigate possible overlap between *in situ* and accreted clusters. In a companion paper (Kruijssen et al. 2020), we extend this analysis, combining the orbital properties of GC sub-groups with their ages and metallicities to predict the properties of their progenitor galaxies.

The paper is organized as follows. Section 2 describes the E-MOSAICS simulations and the analysis of their results. Section 3 presents the main results of this work, comparing the orbital properties of the simulated GC populations with those of the Milky Way GCs. Finally, we discuss and summarize our findings in Section 4.

[1]The age–metallicity relation of the Milky Way GCs appears to be bifurcated, with the young, metal-poor branch thought to originate from the accretion of satellite galaxies and their GCs (Marín-Franch et al. 2009; Forbes & Bridges 2010; Leaman et al. 2013; Kruijssen et al. 2019b).

2 METHODS

2.1 Simulations

The E-MOSAICS project is a suite of cosmological, hydrodynamical simulations of galaxy formation in the Λ cold dark matter cosmogony, which includes a subgrid model for star cluster formation and evolution (we refer the reader to these works for a full description of the models and simulations Pfeffer et al. 2018; Kruijssen et al. 2019a). E-MOSAICS couples MOSAICS star cluster model (Kruijssen et al. 2011; Pfeffer et al. 2018) to the Evolution and Assembly of GaLaxies and their Environments (EAGLE) model for galaxy formation (Schaye et al. 2015; Crain et al. 2015). The EAGLE model reproduces a wide range of galaxy properties, including the redshift evolution of galaxy stellar masses, specific star formation rates and sizes (Furlong et al. 2015, 2017), galaxy luminosities and colours (Trayford et al. 2015), their cold gas properties (Lagos et al. 2015, 2016; Bahé et al. 2016; Marasco et al. 2016; Crain et al. 2017), and the chemical abundance patterns observed in the Milky Way (Mackereth et al. 2018; Hughes et al. 2020).

The MOSAICS model treats star cluster formation and evolution in a subgrid fashion, such that clusters are 'attached' to stellar particles. Star clusters are spawned at the time of formation of a stellar particle and adopt the basic properties of their host particle (positions, velocities, ages, abundances). The formation (numbers, masses) and evolution (mass-loss) of clusters is governed by local properties within the simulations (gas density and pressure, tidal field). MOSAICS adopts a cluster formation model (Kruijssen 2012; Reina-Campos & Kruijssen 2017) that has been shown to reproduce the observed properties of young star cluster populations in nearby galaxies (Pfeffer et al. 2019b). Following their formation, star clusters may then lose mass due to stellar evolution (according to the EAGLE model), tidal shocks, two-body relaxation or may be completely removed due to dynamical friction in the host galaxy (the latter is treated in post-processing, meaning particle orbits are not modified).

In this work, we analyse the volume-limited set of 25 simulations of Milky Way-mass haloes ($M_{\rm vir} \approx 10^{12}\,{\rm M}_\odot$) from the E-MOSAICS project (Pfeffer et al. 2018; Kruijssen et al. 2019a). The haloes were drawn from the high-resolution 25 cMpc volume EAGLE simulation (Recal-L025N0752; Schaye et al. 2015) and resimulated in a zoom-in fashion with the same parameters as the parent volume (a Planck Collaboration I 2014 cosmology, the 'recalibrated' EAGLE model and initial baryonic particle masses of $\approx 2.25 \times 10^5\,{\rm M}_\odot$). In total, 29 snapshots are produced between $z = 20$ and $z = 0$ for each simulation. Bound galaxies (subhaloes) are identified at each snapshot using the SUBFIND algorithm (Springel et al. 2001; Dolag et al. 2009) and merger trees for the subhaloes are created using the method described in Pfeffer et al. (2018).

2.2 Analysis

We limit GCs in the simulations to star clusters with masses $>5 \times 10^4\,{\rm M}_\odot$ at $z = 0$ and metallicities $-2.5 < {\rm [Fe/H]} < -0.5$. This selection is similar to the properties of Milky Way star clusters for which orbital properties (e.g. Myeong et al. 2018d; Baumgardt et al. 2019; Massari et al. 2019) and ages have been determined (Forbes & Bridges 2010; Dotter et al. 2010; Dotter, Sarajedini & Anderson 2011; VandenBerg et al. 2013). The upper metallicity limit also mitigates the oversurvival of metal-rich clusters in the simulations (see Kruijssen et al. 2019a, for discussion).

We calculate peri-($r_{\rm peri}$) and apocentres ($r_{\rm apo}$) for the orbits of these GCs at $z = 0$ and at the snapshot immediately after the stellar particle was formed (the 'initial' value) following the method described in Mackereth et al. (2019, see section 2.4).[2] Clusters with unbound orbits at a given snapshot are disregarded, since their orbital parameters cannot be determined. Eccentricities of the orbits are calculated as $e = (r_{\rm apo} - r_{\rm peri})/(r_{\rm apo} + r_{\rm peri})$.

The angular momentum and total energy of the GCs are calculated at $z = 0$ as follows. For the z-component of the angular momentum, L_z, we first rotate each galaxy to align the total angular momentum of all the bound stars (as calculated by SUBFIND) with the z-axis, assuming that it corresponds to the symmetry axis of the potential. We verified that this is typically the case for galaxies with a clear disc-like morphology. The value of L_z for each GC is then obtained by projecting its total angular momentum vector on to the z-axis. The total energy is obtained by adding the kinetic energy to the gravitational potential energy at the position of each object in the $z = 0$ snapshot. The gravitational potential is calculated by doing a direct sum over the contributions from all the particles in the simulation box. Both the angular momentum and the total energy are expressed per unit mass.

In order to trace accretion events of GCs on to the main galaxy during the simulations, stellar particles that are bound to the main galaxy at $z = 0$ must first be associated with a 'parent' galaxy or branch in the merger tree. For particles bound to subhaloes in the same branch both prior to and after star formation occurs, association is trivial (and stars/GCs are clearly formed *in situ* or are accreted). When a particle changes galaxy branch between the snapshots prior to and after star formation (i.e. during a galaxy merger), associating it to a parent galaxy is less straightforward. The maximum time between snapshots for the simulations is 1.35 Gyr (at $z \approx 0$), much larger than the typical dynamical time-scale for a particle in the central subhalo ($\sim$100 Myr at a galactocentric radius of 10–20 kpc in a Milky Way-mass halo, depending on redshift and galaxy mass). Therefore, a gas particle may be accreted from a satellite and become dynamically associated with the central subhalo on a time-scale shorter than that between snapshots. For this reason, we define the parent subhalo as the subhalo the particle was bound to at the snapshot $<$100 Myr prior to the particle becoming a star, if one exists, and otherwise at the snapshot immediately after star formation.[3] Where multiple snapshots fall within 100 Myr prior to star formation (which is possible at $z > 8$), we define the parent subhalo as the subhalo with the lowest branch mass (generally the earliest accreted branch). To define the accretion event during which a GC was accreted into the main galaxy, we trace the merger tree from the parent subhalo to the main branch of the merger tree for the central galaxy at $z = 0$.

In situ GCs are also defined based on their parent subhalo, with the addition of two criteria: a galactocentric radius selection and the requirement that the particle was bound to the main galaxy branch prior to becoming a star particle. This allows us to define a sample of *clearly in situ* GCs and excludes those with an ambiguous origin. Following Sanderson et al. (2018), we define *in situ* star particles as those located within 30 kpc of the main galaxy at the snapshot immediately after star formation. This selection therefore excludes (e.g.) stellar particles that may have formed in the tidal tails of accreting galaxies, but which are not bound to the incoming satellite at the time of formation as determined by the SUBFIND algorithm, and would otherwise be classified as *in situ* formation. The combination of the radius selection and being bound to the central galaxy prior to star formation excludes $\approx$12 per cent of GCs with an ambiguous origin (the majority of which, 7 per cent, do not pass the radius cut), which would be classed as *in situ* formation by the merger tree criteria alone.

To compare the *in situ* GCs from the simulations against the Milky Way GCs (Section 3.4), we select galaxies from the 25 zoom-in simulations with $z = 0$ properties most similar to the Milky Way, excluding spheroidal galaxies and those with late major mergers. We first select disc-dominated galaxies with a disc-to-total stellar mass $D/T > 0.45$ (equivalent to the fraction of kinetic energy invested in ordered corotation $\kappa_{\rm co} = 0.4$, Correa et al. 2017; Thob et al. 2019). Disc stars are selected following Abadi et al. (2003) and Sales et al. (2012) and require an orbit circularity parameter $J_z/J_{\rm circ} > 0.5$ (i.e. the ratio of the specific angular momentum perpendicular to the disc to that of a circular orbit with the same energy). We also remove galaxies that have on-going (at $z = 0$) or late major mergers ($z < 0.8$) with a stellar mass ratio $M_2/M_1 > 1/4$ (where $M_2 < M_1$). These criteria leave us with 14 galaxies from the sample for which we compare *in situ* GCs. For the accreted GCs we use all 25 Milky Way-mass galaxies, since we do not expect the GC orbits to be strongly affected by the present-day galaxy morphology.

3 RESULTS

3.1 Milky Way GCs

For reference and comparison with the simulations, in Fig. 1 we show the orbital properties of Milky Way GCs. In the upper panel we show their apocentres and eccentricities, while in the lower panel we show their total energy (normalized to $E_{\rm norm} = -1$ at $L_z = 1500\,{\rm km\,s^{-1}}$ kpc for comparison with the simulations, see Section 3.2.2) and z-component of the angular momentum. The apocentres and eccentricities were taken from Baumgardt et al. (2019). The angular momentum was calculated using the velocities and distances from Baumgardt et al. (2019), and the energies were obtained assuming the McMillan (2017) potential model of the Milky Way.[4]

We take the groupings into possible progenitors from Massari et al. (2019, M-D: main-disc, M-B: main-bulge, L-E: low energy/Kraken, G-E: *Gaia* Sausage/Enceladus, Sag: Sagittarius dSph, H99: Helmi et al. 1999 streams, Seq: Sequoia, H-E: high energy), with a few modifications. Based on the GC ages and metallicities in the compilation of Kruijssen et al. (2019b), we updated the group associations of E3 to M-D, NGC 6441 to M-B and labelled Palomar 1 (H-E) and NGC 6121 (L-E) as uncertain (Palomar 1 has an age/metallicity consistent with young satellite GCs but an orbit consistent with disc GCs, while NGC 6121 has an age placing it intermediate between the accreted and *in situ* branches in age–metallicity space). See Kruijssen et al. (2020) for further discussion about the memberships of these GCs. We note that the division of GCs into accretion groups is always somewhat

[2]This method assumes the potential is approximately spherically symmetric, which is not assumed for the calculation of E and L_z below. However, this is a reasonable assumption in the region where the disc/bulge does not dominate the potential, since the effect of dissipation in baryonic simulations makes dark matter haloes (which dominate the potential in the galaxies) significantly more spherical than in dark matter only simulations (Dubinski 1994; Kazantzidis et al. 2004; Springel, White & Hernquist 2004).

[3]Note that, depending on the timing of the galaxy merger relative to the snapshots, the method could potentially underassociate particles to an accreting galaxy. This method would be improved simply by taking a higher frequency of snapshots.

[4]Baumgardt et al. (2019) assume the Irrgang et al. (2013) potential model to integrate the orbits. However, they note that there was little difference in the results when assuming the McMillan (2017) model.

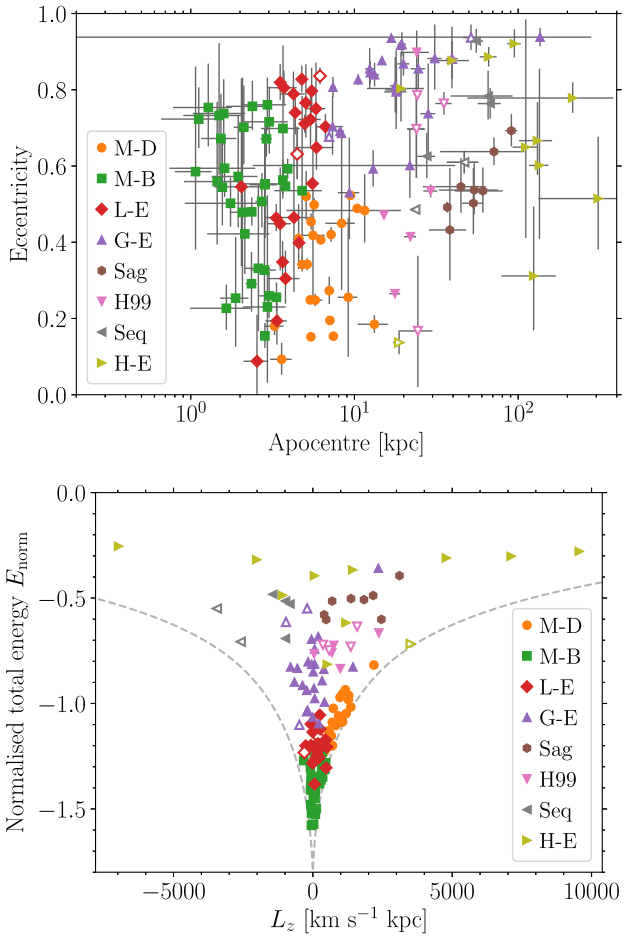

Figure 1. Orbital properties of Milky Way GCs. The upper panel shows apocentres and eccentricities (from Baumgardt et al. 2019) while the lower panel shows the normalized total energy (normalized at $L_z = 1500\,{\rm km\,s^{-1}}$ kpc) and the z-component of the angular momentum. GC groupings were taken from Massari et al. (2019, M-D: main-disc, M-B: main-bulge, L-E: low energy/Kraken, G-E: *Gaia* Sausage/Enceladus, Sag: Sagittarius dSph, H99: Helmi et al. (1999) streams, Seq: Sequoia, H-E: high energy; with some minor changes, see the text). Open symbols show clusters with uncertain group designations.

uncertain, in particular given possible overlap of the groups in orbital space, and subject to change given new information. We touch on this point in Section 3.3, where we present the orbital properties of GCs accreted by individual galaxies. In general, we will compare the median properties of possible GC accretion groups, since the median properties are relatively robust to the uncertainties of group classification (see also Kruijssen et al. 2020, where we explicitly take this into account).

Though the L-E and G-E GC groups have similar age–metallicity relations (Massari et al. 2019), the groups have very different orbital properties, suggesting different origins. The L-E group has a median apocentre of 4.4 kpc and median eccentricity of 0.68, while the G-E group has a median apocentre of 18.0 kpc and median eccentricity of 0.81. The groups also occupy a very different range in eccentricities: ≈0.1–0.85 for the L-E group, compared with ≈0.5–0.95 for the G-E group. The GCs from lower mass progenitors are generally found at larger apocentres (median of 24.0 kpc for the H99 streams, 37.3 kpc for Sequoia and 53.6 kpc for Sagittarius).

3.2 Orbital trends with mass and merger redshift

3.2.1 Apocentre and eccentricity

In Fig. 2, we compare the apocentres and eccentricities of accreted GCs at $z = 0$ from the 25 Milky Way-mass galaxies (with the exception of the bottom left panel, which shows *in situ* GCs and is discussed in Section 3.4). The GCs of accreted galaxies are divided into panels by the satellite galaxy stellar mass at accretion (with increasing mass from upper to lower rows) and the merger redshift (with decreasing merger redshift from left to right columns). We give the median apocentres and eccentricities for each panel in Tables 1 and 2, respectively. Note that, because the effect of dynamical friction on GC orbits is not included, apocentres may be larger than they should be realistically, particularly for GCs that orbit at small galactocentric radii. For a GC with mass $10^5\,{\rm M}_\odot$ on a circular orbit at 2 kpc in MW04, the typical dynamical friction timescale is $t_{\rm df} \approx 100$ Gyr. Therefore, for a typical GC, this correction is not relevant and only applicable for massive GCs ($\gtrsim 10^6\,{\rm M}_\odot$, for which $t_{\rm df} \lesssim 10$ Gyr). However, what cannot be captured in the model is the effect of shrinking orbits within the host satellite prior to merging, which could potentially result in GCs being deposited at smaller apocentres through later tidal stripping. Another factor which may affect the resulting orbits is the size of the galaxies. Low-mass galaxies ($M_* < 10^9\,{\rm M}_\odot$) in the EAGLE model are slightly too extended compared to observed galaxies (Schaye et al. 2015; Furlong et al. 2017), though the comparison is improved for the 'Recalibrated' EAGLE model (used in this work) relative to the lower resolution 'Reference' model. Galaxies which are too extended may suffer from premature tidal disruption relative to more compact galaxies, thus resulting in larger apocentres due to the decreased efficiency of dynamical friction.

For the accreted GCs, at fixed galaxy mass, there is a strong trend of apocentre with merger redshift, with earlier mergers having smaller apocentres. At fixed merger redshift, apocentres also become smaller with increasing satellite galaxy mass, i.e. mergers with more massive accretors deposit their clusters and stars at smaller apocentres. Both trends persist across all galaxy mass and merger redshift ranges, respectively (Table 1). The trend with redshift appears reversed for the most massive galaxies ($M_* > 10^{9.5}\,{\rm M}_\odot$) which is likely due to poor galaxy number statistics in the 0.5−1.1 redshift range (two galaxies). With such small numbers sampling of the galaxy mass function becomes important due to the correlation of galaxy mass and median apocentre after accretion. Comparing just the most massive accreted galaxy in each redshift range ($M_* \approx 10^{10}\,{\rm M}_\odot$ for both) we find the trend still holds; the galaxy accreted at $z \approx 1$ has a median GC apocentre of 9 kpc, while the galaxy accreted at $z \approx 0$ has a median apocentre of 19 kpc. Other factors, such as the initial orbital conditions of the mergers, may also affect the correlations when sampling of galaxies is poor.

We find no trends for M_* or z_M with the median eccentricity of the GC orbits [Table 2; the interquartile range (IQR) of eccentricity for individual galaxies does however correlate with galaxy mass, which we discuss further in Section 3.3]. The uncertainties of the medians range from 0.015 to 0.1 and thus most bins in redshift and galaxy mass are consistent with the median for all accreted GCs (0.71 ± 0.01). The median eccentricity for accreted GCs in the simulations (0.71) is in extremely good agreement with the median for accreted Milky Way GCs (0.70 ± 0.03 for those not associated with M-D or M-B; Fig. 1).

The cause of the decrease of GC apocentres with increasing progenitor satellite mass and merger redshift is the competition of dynamical friction between the central and satellite galaxies (which

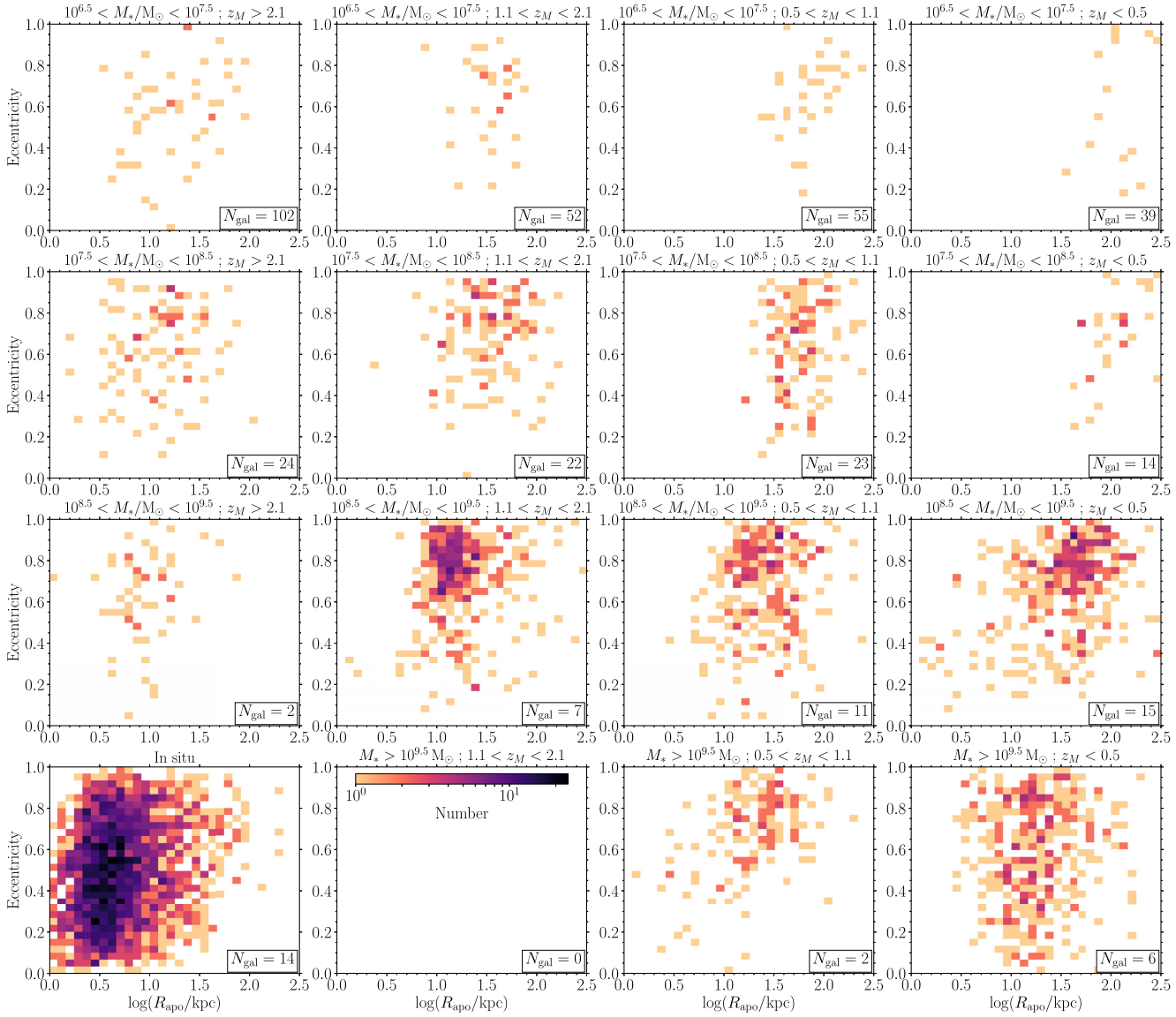

Figure 2. Eccentricities and apocentres of accreted GCs at $z = 0$, stacked by satellite galaxy stellar mass (galaxy mass increases from top to bottom) and merger redshift (early to late mergers from left to right) in the 25 Milky Way-mass galaxies from the E-MOSAICS simulations. The bottom left panel shows the eccentricities and apocentres for *in situ* GCs in disc-dominated galaxies at $z = 0$. The colour scale of the histograms is logarithmic, normalized to the maximum in the *in situ* panel. The inset N_{gal} shows the number of galaxies which satisfy the M_* and z_M selection criteria (for the low-mass galaxies, $10^{6.5} < M_*/\,\mathrm{M}_\odot < 10^{7.5}$, not all galaxies contribute GCs).

Table 1. Median apocentres (kpc) for GCs of all accreted galaxies in bins of satellite stellar mass and accretion redshift (Fig. 2).

M_* ($\mathrm{M}_\odot$)	z_M			
	>2.1	2.1–1.1	1.1–0.5	<0.5
$10^{6.5}$–$10^{7.5}$	17.6	35.9	66.6	117.4
$10^{7.5}$–$10^{8.5}$	13.7	32.6	54.0	100.7
$10^{8.5}$–$10^{9.5}$	8.2	15.0	24.3	41.4
$>10^{9.5}$			21.9	16.5

Table 2. Median eccentricities for GCs of all accreted galaxies in bins of satellite stellar mass and accretion redshift (Fig. 2).

M_* ($\mathrm{M}_\odot$)	z_M			
	>2.1	2.1–1.1	1.1–0.5	<0.5
$10^{6.5}$–$10^{7.5}$	0.59	0.70	0.70	0.62
$10^{7.5}$–$10^{8.5}$	0.66	0.74	0.68	0.74
$10^{8.5}$–$10^{9.5}$	0.66	0.76	0.72	0.73
$>10^{9.5}$			0.73	0.62

occurs self-consistently in the simulations) and tidal stripping of the satellite galaxy. Dynamical friction occurs most efficiently as the merging galaxies approach a 1:1 mass ratio (Chandrasekhar 1943; Binney & Tremaine 2008). Therefore, for a given central galaxy mass, higher mass galaxies will sink to the centre of the central galaxy on a shorter time-scale. Conversely, lower mass galaxies would also sink to the centre of the central galaxy given enough time, but are tidally stripped, and eventually completely disrupted, on a time-scale much faster than the time-scale for dynamical friction due to their lower binding energies. At later times the central galaxy (or dark

matter halo) is more massive and therefore at a given satellite galaxy mass and size, tidal stripping of both field stars and GCs occurs at larger galactocentric radii at lower redshifts. At the same time, dynamical friction is also less effective at later times as the mass ratio decreases.

Comparing the results of Fig. 2 with Fig. 1, we can estimate approximate merger times for the progenitors of the different GC groups in the Milky Way. The L-E group has a median apocentre of 4.4 kpc (range of 2.7–8.7 kpc), suggesting it was most likely accreted into the Milky Way at early times ($z > 2$). Late accretion ($z < 1$) is disfavoured because GCs could only be deposited in galaxies at such small apocentres (<10 kpc) during major mergers, for which there is no evidence in the Milky Way (Wyse 2001; Hammer et al. 2007; Stewart et al. 2008; Kruijssen et al. 2019b). The L-E group also favours galaxy masses $M_* > 10^{7.5}\,\mathrm{M}_\odot$, since clusters accreted from lower mass galaxies at $z > 2$ typically have apocentres >10 kpc (Table 1) and cover a much wider range in apocentres (at $z > 2$ the IQR of the apocentres decreases from 27 kpc in the lowest mass bin to 6 kpc in the highest mass bin).

The *Gaia* Sausage/Enceladus accretion event has been suggested to have a stellar mass $\sim 10^9\,\mathrm{M}_\odot$ and accreted ∼9–10 Gyr ago or later (Belokurov et al. 2018; Haywood et al. 2018; Helmi et al. 2018; Myeong et al. 2018d, 2019; Bignone et al. 2019; Conroy et al. 2019; Mackereth et al. 2019), though in Kruijssen et al. (2020) we find a mass $M_* \approx 10^{8.4}\,\mathrm{M}_\odot$. The median apocentre of G-E GCs (18 kpc) does not itself place a constraint on the galaxy mass, since such apocentres are achievable (Table 1) through both early, low-mass mergers ($z_M > 2$, $M_* < 10^{7.5}\,\mathrm{M}_\odot$) and late, major mergers ($z_M < 0.5$, $M_* > 10^{9.5}\,\mathrm{M}_\odot$). Further information is therefore required to derive a merger time for G-E due to this mass-merger redshift degeneracy. However, a mass range $10^{7.5} < M/\mathrm{M}_\odot < 10^{9.5}$ suggests a merger between redshifts ≈1–2 (8–10.5 Gyr ago).

The Sagittarius GCs have a median apocentre of 53.6 kpc (Fig. 1), while the Sagittarius dwarf galaxy has a total progenitor luminosity of $M_\mathrm{V} \sim -15.1$ to -15.5 (Niederste-Ostholt et al. 2010), or a stellar mass ~ 2–$3 \times 10^8\,\mathrm{M}_\odot$ for a stellar mass-to-light ratio of $M/L_\mathrm{V} = 2\,(\mathrm{M/L})_\odot$.[5] From the results of Fig. 2 and Table 1, these parameters imply a merger redshift $z_M < 1$, consistent with the status of Sagittarius currently undergoing tidal disruption (Ibata, Gilmore & Irwin 1994; Velazquez & White 1995; Ibata et al. 1997).

The H99 stream and Sequoia GC groups both have median apocentres around 30 kpc (24.0 and 37.3 kpc, respectively). However, the derived stellar masses differ by an order of magnitude. Koppelman et al. (2019a) find a stellar mass for the H99 stream progenitor of $M_* \sim 10^8\,\mathrm{M}_\odot$, while Myeong et al. (2019) find a stellar mass for Sequoia of $M_* \sim 5$–$70 \times 10^6\,\mathrm{M}_\odot$. This implies a merger redshift $z_M > 1$ for both galaxies: $z_M \sim 2$ for the H99 stream and $z_M \sim 1.5$ for Sequoia (a lower mass for the H99 stream progenitor, e.g. $10^7\,\mathrm{M}_\odot$, would not significantly change this result), consistent with the youngest ages of probable H99 stream and Sequoia GCs ($\gtrsim$11 Gyr, Koppelman et al. 2019a; Massari et al. 2019; Myeong et al. 2019).

3.2.2 *Energy and angular momentum*

In Fig. 3, we show the normalized total energy (E_norm) and z-component of the angular momentum (L_z) for GCs at $z = 0$ for the same panels in Fig. 2. Since the circular orbit curve differs for each galaxy depending on the mass profile, we normalize the energy for the GCs of each galaxy by the absolute value of the energy of a circular orbit with $L_z = 1500\,\mathrm{km\,s^{-1}\,kpc}$[6] such that the circular orbit curves are approximately aligned for all galaxies. Given that the total energy and apocentre for an orbit in a galaxy are related, the typical energy for accreted clusters follows the same trend with galaxy mass and accretion redshift as for the typical apocentre. At fixed satellite mass, GCs from earlier mergers are more tightly bound (lower total energy) than those accreted later; while at fixed merger redshift, GCs from higher mass satellite galaxies are more tightly bound than those from lower mass satellites.

As for eccentricities (Fig. 2), we find no trend for L_z with mass or merger redshift. However, the one exception is late ($z < 0.5$), massive ($M_* > 10^{9.5}\,\mathrm{M}_\odot$) mergers, which generally show prograde motion due to the spin axis of the galaxy becoming aligned with the axis of the merger. The range in L_z increases for lower mass mergers, simply because GCs from lower mass mergers have higher energies, increasing the possible range in L_z.

3.3 Individual accreted galaxies

In Figs 4 and 5, we show the apocentre-eccentricity and E_norm–L_z projections, respectively, for GCs of individual accreted galaxies at $z = 0$. The figures show accreted galaxies with stellar masses $\sim 10^{8.4}\,\mathrm{M}_\odot$, similar to the masses which we find for *Gaia* Sausage/Enceladus and Kraken in Kruijssen et al. (2020) and that of the Sagittarius dwarf (Niederste-Ostholt et al. 2010). Mergers often exhibit a tail of GCs to higher apocentres and energies (e.g. panels *a*, *e*, *g*, and *l*). Such objects would be problematic when dividing GCs into accretion groups based on orbital properties, since any overlap with other accretion events may result in incorrect group association.

As discussed in Section 3.2, for a given satellite mass, earlier merger events tend to result in smaller apocentres (Fig. 4) and lower total energies (Fig. 5). The galaxies in Fig. 4 also show a diversity in the extent of their GC eccentricity distributions. In Fig. 6, we compare the IQR of GC eccentricities with the stellar mass of all galaxies in the figure. Higher mass galaxies tend to have a larger IQR of GC eccentricities. This could be the result of a broader distribution of velocities of GCs within massive galaxies, or the merger process for massive galaxies significantly altering GC orbits (the snapshot frequency of the simulations is not sufficient to investigate this further). We also colour the points in the figure by the galaxy merger redshift. At a given galaxy mass, early mergers also tend to result in a larger range of eccentricities at $z = 0$. This could be the result of frequent mergers in the early Universe dynamically heating the orbits, increasing the spread in eccentricities, while later mergers have had significantly less time for such a process. Alternatively (or additionally), higher merger ratios (i.e. earlier mergers at fixed galaxy mass) may simply generally result in a larger distribution of eccentricities.

With an IQR for the GC eccentricities of 0.3 and the requirement of an early merger ($z > 2$) from the apocentres of the GC orbits (Section 3.2.1), this result therefore favours an accretion event with a mass $M_* \gtrsim 10^{8.3}\,\mathrm{M}_\odot$ for the L-E group. G-E GCs have an IQR for eccentricities of 0.18 which suggests a mass $M_* \lesssim 10^{8.5}\,\mathrm{M}_\odot$, though it gives no constraint on accretion time. Accretion events with tightly clustered eccentricities (IQR ∼0.1; e.g. Sagittarius in Fig. 1, with an IQR of 0.07), generally occur at later times ($z_M \lesssim 1$;) and at larger apocentres (>10 kpc). Of the galaxies in Fig. 4, panels

[5] Assuming an age of 8 Gyr and [Fe/H] = −0.5 (Bellazzini et al. 2006) for a simple stellar population with the Flexible Stellar Population Synthesis model (Conroy, Gunn & White 2009; Conroy & Gunn 2010).

[6] In practice, we use the minimum E for all star particles with $L_z > 1500\,\mathrm{km\,s^{-1}\,kpc}$.

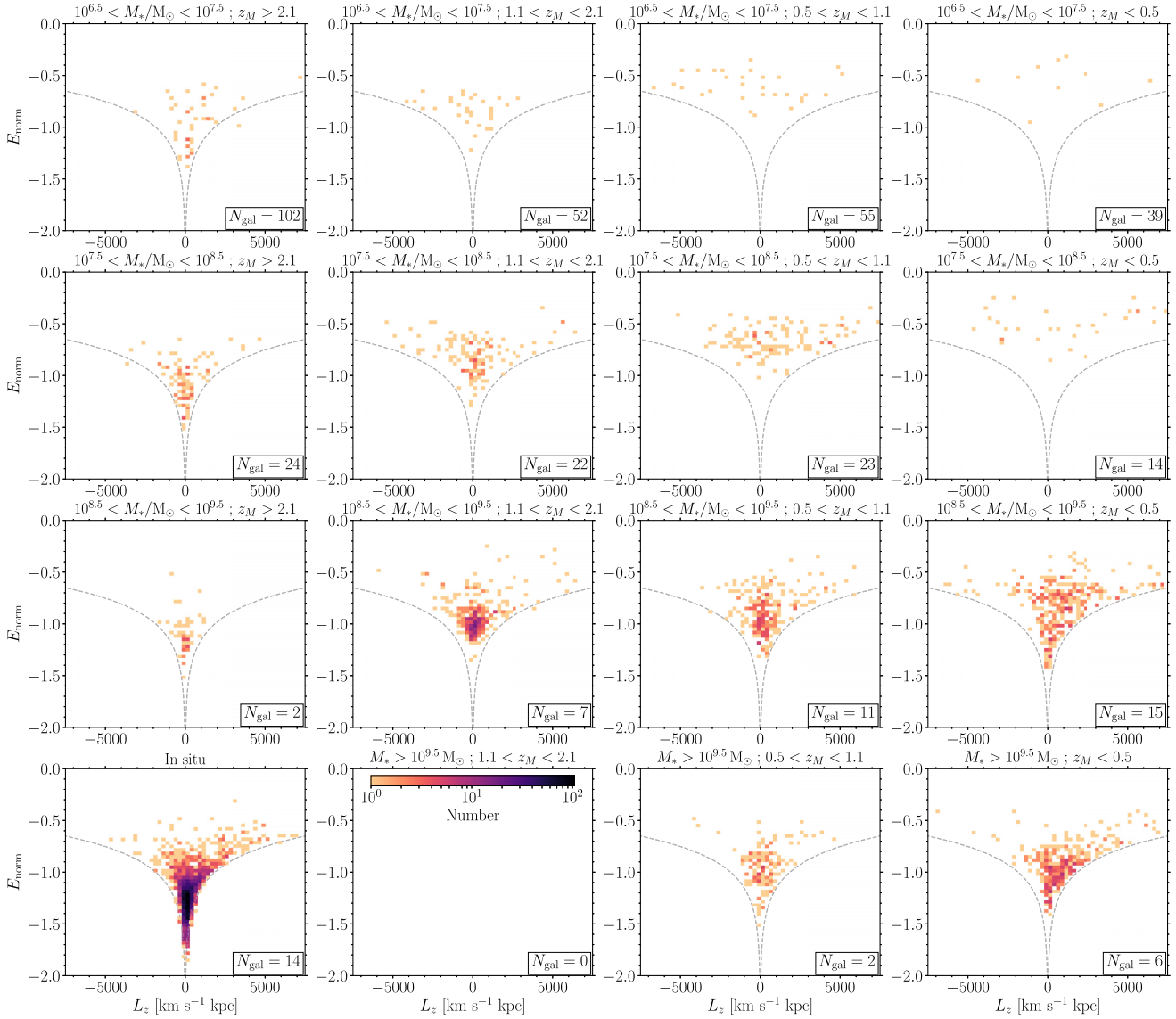

Figure 3. Normalized total energy, E_{norm} (normalized to $E_{\mathrm{norm}} = -1$ at $L_z = 1500\,\mathrm{km\,s^{-1}\,kpc}$), and the z-component of the angular momentum, L_z, of accreted GCs at $z = 0$. Panel layout is as in Fig. 2, with galaxies stacked by satellite galaxy stellar mass (galaxy mass increases from top to bottom) and merger redshift (early to late mergers from left to right). The bottom left panel shows E_{norm} and L_z for *in situ* GCs in disc-dominated galaxies at $z = 0$. The colour scale of the histograms is logarithmic, normalized to the maximum in the *in situ* panel. The dashed lines approximately indicate the circular orbit curve for reference (this is not a fit, since the circular orbit curve differs from galaxy to galaxy).

t (IQR = 0.06), v (IQR = 0.16) and w (IQR = 0.02) have accreted galaxies producing tidal streams at $z = 0$ (cross-matching with the list of galaxies producing streams from Hughes et al. 2019, and rerunning the analysis for those galaxies not previously included in their sample). This implies that earlier accretion events with a small distribution in eccentricity (e.g. panel h, IQR = 0.16) also produced tidal streams which have since dispersed.

In Fig. 5, GCs of a given accreted galaxy are generally tightly clustered in normalized energy. The typical IQR in E_{norm} for GCs of a given galaxy is 0.2 (and ranges from 0.04 to 0.34), which does not vary with merger redshift, though some merger events exhibit a tail of GCs to higher energies (e.g. panel l). This typical IQR in E_{norm} is consistent with the range in energies for G-E (IQR of 0.2) and L-E GCs (IQR of 0.09) and further suggests they are indeed separate merger events.

3.4 *In situ* GCs

In the bottom left panels of Figs 2 and 3, we compare the orbital properties of GCs formed *in situ* within the central galaxies in the simulations. In order to limit the comparison to morphological analogues of the Milky Way, we only compare the GCs of galaxies which are disc-dominated ($D/T > 0.45$) at $z = 0$ and have not had a major merger since $z < 0.8$.

The bottom left panel of Fig. 2 shows the comparison of apocentre and eccentricity. The *in situ* GCs are generally very centrally concentrated, with a median apocentre of 4.3 kpc. They have a median eccentricity of 0.49, but with a large internal spread, spanning the full eccentricity range. The 14 galaxies individually span a range in median eccentricity of 0.42-0.58. This range is in very good agreement with the median for *in situ* Milky Way GCs (Fig. 1), for

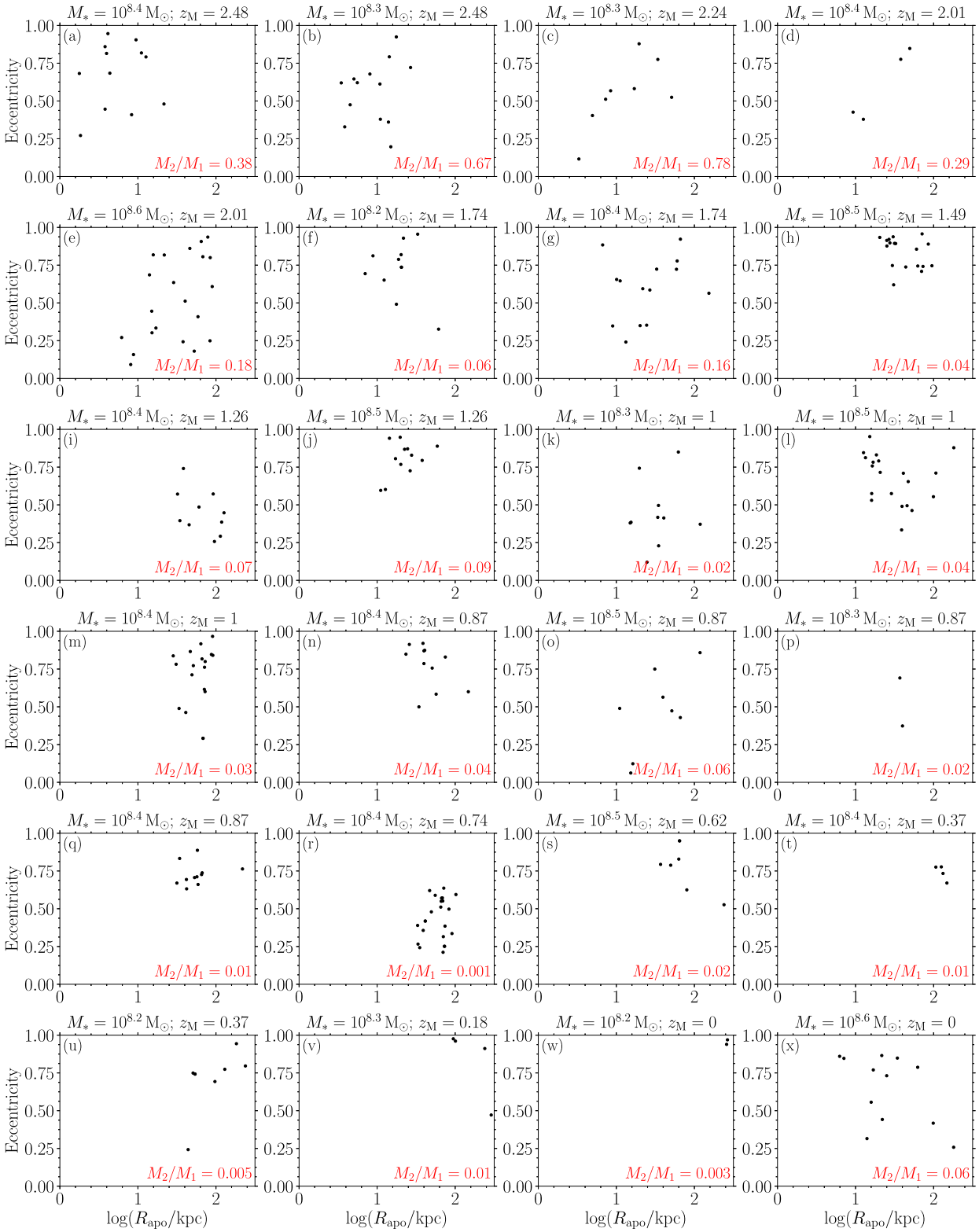

Figure 4. Eccentricity and apocentre for GCs of individual accreted galaxies with stellar masses between $10^{8.1}$ to $10^{8.6}\,M_\odot$. Galaxies are ordered in the figure by decreasing merger redshift (left to right, top to bottom). The stellar mass merger ratio is shown in the bottom right of each panel.

which the combined M-D+M-B sample has a median eccentricity of 0.48 ± 0.03. It is unlikely this result could be affected by dynamical friction (which is not included for the orbits of the simulated GCs), since *N*-body simulations which include a live host galaxy do not find strong circularization of orbits by dynamical friction (van den Bosch et al. 1999; Hashimoto, Funato & Makino 2003).

A related question is whether eccentricities of GCs are set at the time of formation, or if clusters formed on nearly circular orbits

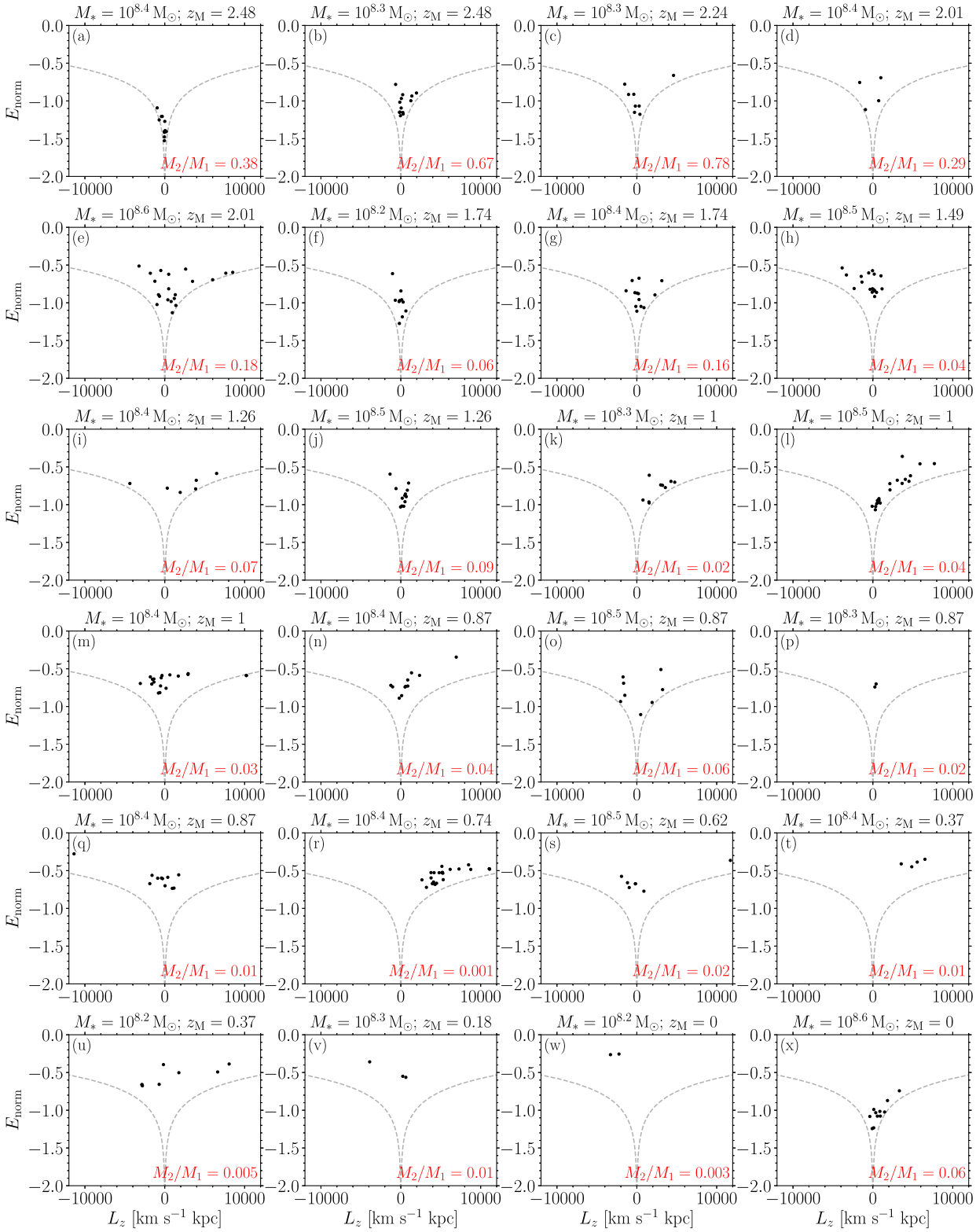

Figure 5. Normalized total energy ($E_{\rm norm}$) and the z-component of the angular momentum (L_z) for the GCs of individual accreted galaxies as in Fig. 4. The dashed lines approximately indicate the circular orbit curve for reference.

which later became more eccentric (e.g. due to galaxy mergers). Due to the frequency of the snapshots, we cannot calculate orbits for all clusters at the time of formation. Limiting the sample to GCs formed <20 Myr prior to a snapshot ($N = 96$ GCs, compared with 2703 for the total sample in the 14 galaxies), we find that the initial orbits (median eccentricity 0.48) are only marginally more circular than the orbits of the GCs at $z = 0$ (median 0.51). Thus, the median eccentricities of *in situ* GCs in the disc-dominated galaxies

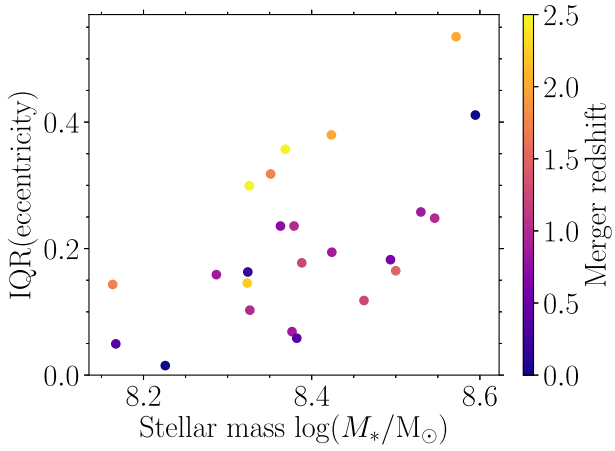

Figure 6. The IQR of GC eccentricities as a function of galaxy stellar mass for the galaxies in Fig. 4, with points coloured by the galaxy merger redshift. Massive and early mergers tend to have a larger range of eccentricities.

change very little over time. However, we note that the orbits of individual GCs may significantly change between formation and $z = 0$; in fact, the initial and final eccentricities of individual GCs are not correlated. This simply follows from galactic dynamics, such that individual orbits can change substantially even if the population statistics remain the same.

The comparison between $E_{\rm norm}$ and L_z for the *in situ* GCs in the disc-dominated simulations is shown in the bottom left panel of Fig. 3. In situ GCs have predominantly prograde rotation (as expected) and generally lower energies than accreted clusters (cluster formation is biased to the galactic centre, where gas pressures are generally highest, see Pfeffer et al. 2018). However, *in situ* GCs also show a tail to high energies, and some even exhibit very retrograde orbits (counter-rotating relative to the disc). In Fig. 7, we compare the median metallicity (upper panel) and age (lower panel) for *in situ* GCs in each cell of the $E_{\rm norm}$–L_z histogram. The high energy and retrograde *in situ* GCs tend to have low metallicities ([Fe/H] $\lesssim -1$) and formed in the early universe (ages $\sim$12 Gyr) when significant galaxy mergers were common, enabling the redistribution of cluster orbits or, in the case of very significant mergers, potentially changing the orientation of the angular momentum vector of the galaxy (invalidating the assumption of conservation of L_z). A small number of retrograde GCs at high energies also have very young ages ($\sim$6 Gyr), most likely being misclassified GCs formed from gas accreted from infalling satellites.

Old, low-metallicity, *in situ* GCs therefore show significant overlap with accreted GCs in E–L_z space. *In situ* and accreted GCs at low metallicities also overlap in their old ages (Kruijssen et al. 2019a) and α-abundances (Hughes et al. 2020), meaning a combination of orbits, ages and chemistry may not be sufficient to unambiguously distinguish the origin of individual GCs in such cases (see also Koch & Côté 2019).

In situ GCs at low energies or on prograde orbits are generally relatively metal rich ([Fe/H] ~ -0.5, i.e. near the upper metallicity limit we adopt). The GCs on nearly circular, prograde orbits at high energies and high L_z also tend to be relatively young (ages $<$10 Gyr) compared to the GCs at low energies (ages $\sim$12 Gyr), due to the inside-out nature of disc formation (e.g. Larson 1976; Matteucci & Francois 1989; Burkert, Truran & Hensler 1992; Muñoz-Mateos et al. 2007). For *in situ* GCs in the simulations, outer disc GCs with apocentres $>$10 kpc (at $z = 0$) represent $\approx$11 per cent of GCs with very circular orbits (eccentricities $<$0.3). These objects

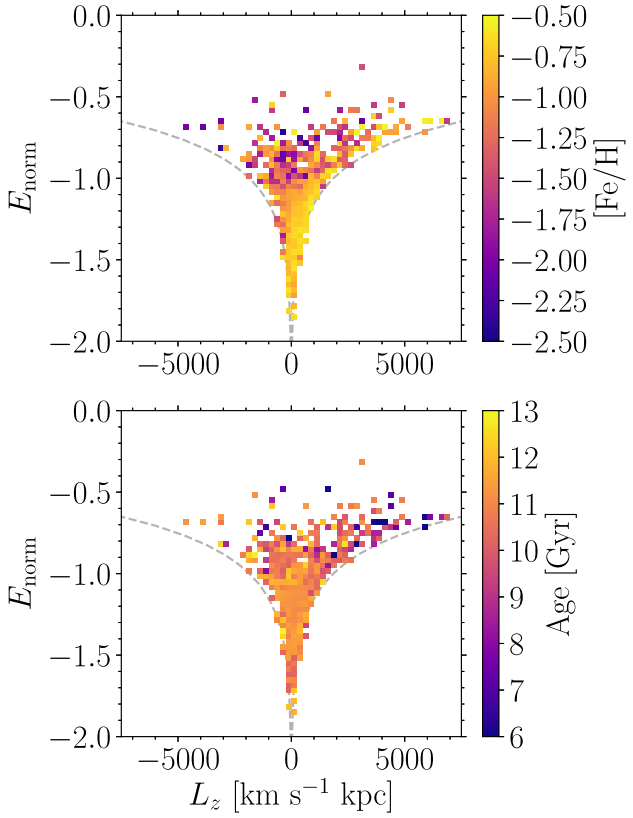

Figure 7. Normalized total energy ($E_{\rm norm}$) and the z-component of the angular momentum (L_z) for *in situ* GCs (as in the bottom left panel of Fig. 3) coloured by the median metallicity (upper panel) and median age (lower panel) of each cell in the 2D histogram.

have a number of possible analogues in the Milky Way, namely Palomar 1, Palomar 5, E3, and NGC 5053 (Baumgardt et al. 2019). The four GCs make up 18 per cent of all Milky Way GCs with eccentricities $<$0.3. In the Massari et al. (2019) list of possible progenitor galaxy associations, E3 was associated with the main disc, NGC 5053, and Palomar 5 are possible associations with the H99 streams and Palomar 1 was listed in the 'high-energy' group (no known progenitor). Of the four, Palomar 1 could be an example of a GC formed *in situ* in the outer Milky Way disc, given its age of $\sim$7 Gyr and metallicity [Fe/H] $= -0.7$ (Forbes & Bridges 2010). Palomar 1 has also previously been classified as a bulge/disc cluster based on its horizontal branch morphology (Zinn 1993; Mackey & van den Bergh 2005).

4 DISCUSSION AND CONCLUSIONS

Analysing the results of the E-MOSAICS simulations of Milky Way-mass galaxies, we find that the orbits (apocentre and total energy, in particular) of GCs deposited by accretion events are sensitive to the satellite galaxy mass and merger redshift. Earlier mergers and larger galaxy masses result in more tightly bound GCs (smaller apocentres). We expect these trends should exist across all host galaxy masses, though the exact relationships between the apocentre or energy of the orbits and satellite mass and merger redshift will differ with host galaxy/halo mass.

Taking advantage of the GC groupings corresponding to probable accretion events defined by Massari et al. (2019), we estimate merger

redshifts based on the apocentres of the GC orbits and the most likely progenitor stellar masses:

(i) For *Gaia* Sausage/Enceladus we find a merger redshift in the range $z_M \approx 1$–2, depending on the assumed stellar mass for the progenitor ($10^{7.5} < M_*/\,\mathrm{M}_\odot < 10^{9.5}$). The small IQR of eccentricities for the G-E group of GCs favour an accretion event with stellar mass $M_* \lesssim 10^{8.5}\,\mathrm{M}_\odot$ (Section 3.3). This is in reasonable agreement with Belokurov et al. (2018), who suggest a merger 8–11 Gyr ago based on the velocity anisotropy of the stellar debris, and Helmi et al. (2018), who suggest a merger ≈10 Gyr ago based on the youngest G-E stars. It is also consistent with the results of Mackereth et al. (2019), who found that galaxy accretion resulting in very eccentric orbits (median eccentricity for the stellar debris of >0.8) only occur for accretion at late times, implying an accretion redshift of $z < 1.5$. We note that Bignone et al. (2019) found a possible G-E analogue in the EAGLE simulations, for which the merger occurred at $z \sim 1.2$.

(ii) For the H99 stream (Helmi et al. 1999) and Sequoia (Myeong et al. 2019) we find $z_M \sim 2$ and 1.5, respectively (and certainly $z_M > 1$). The implied merger times are consistent with the ages of the youngest GCs in each group and the youngest stars (≈11 Gyr old) in H99 (Koppelman et al. 2019a; Massari et al. 2019; Myeong et al. 2019). Based on idealized *N*-body simulations, Kepley et al. (2007) and Koppelman et al. (2019a) suggest the H99 stream progenitor was accreted 5-9 Gyr ago (with lower galaxy masses implying older mergers). Assuming Sequoia and the S1 stream are connected, Myeong et al. (2018a, 2019) suggest an infall time for Sequoia of >9 Gyr ago, in agreement with our result.

(iii) The median apocentre of Sagittarius GCs implies a late merger ($z_M < 1$), in agreement with the dwarf galaxy currently undergoing tidal disruption (Ibata et al. 1994).

(iv) The L-E group (Massari et al. 2019), for which the progenitor stellar debris is yet to be discovered, has the most compact apocentres (median 4.4 kpc) of all (presumably) accreted subpopulations (Fig. 1). Such small apocentres require (Table 1) an early accretion time ($z_M \gtrsim 2$) and a progenitor galaxy mass $>10^{7.5}\,\mathrm{M}_\odot$. Combined with the constraint on merger redshift, the range of GC eccentricities in the L-E group favour an accretion event with stellar mass $M_* \gtrsim 10^{8.3}\,\mathrm{M}_\odot$ (Section 3.3). This is in agreement with the age–metallicity relation of the L-E group GCs (Massari et al. 2019) which indicates a relatively massive progenitor galaxy (Kruijssen et al. 2019a, b) and disfavours *in situ* formation in the Galaxy due to their low metallicities at ages ≈11 Gyr. The implied merger time is also consistent with the age (≈10.5 Gyr) of the youngest L-E GC (or ≈11 Gyr for the second youngest GC Massari et al. 2019).

These results reaffirm the findings of Kruijssen et al. (2019b) that the Milky Way underwent two massive accretion events in its past. We argue that the L-E group is in fact remnants of the Kraken event (see also Forbes 2020; Kruijssen et al. 2020), predicted by Kruijssen et al. (2019b) based on the number of GCs in the satellite branch of the GC age–metallicity distribution and the galaxy mass implied by their age–metallicity relation. The large distribution of eccentricities and small apocentres of Kraken GCs (and thus presumably also its field stars) means that detecting the stellar debris of the merger may be a tough prospect, since there will not be an obvious clustering of stars in orbital space and there may be significant overlap with Milky Way disc stars. Alternatively, with accurate stellar ages, it may be possible to find stars on tightly bound orbits with properties (ages ≈11 Gyr, [Fe/H] ≈ −1.3) similar to the youngest Kraken GCs. Such stars should be significantly younger than *in situ* stars at similar metallicities (or more metal-poor than *in situ* stars at similar ages).

Finally, we investigate the orbits of *in situ* GCs in the simulated galaxies. We find that the median eccentricities of both *in situ* (0.49) and accreted GCs (0.71) in the simulations are in remarkable agreement with the Milky Way GCs (0.48 for M-D+M-B GCs and 0.7 for all other sub-groups combined). This result provides further evidence that a formation mechanism similar to that observed for young star clusters (for reviews, see Portegies Zwart, McMillan & Gieles 2010; Kruijssen 2014; Adamo & Bastian 2018), combined with hierarchical formation and assembly of galaxies, can explain the GC populations observed today (e.g. Elmegreen & Efremov 1997; Kravtsov & Gnedin 2005; Kruijssen 2015; Li et al. 2017; Pfeffer et al. 2018; Kruijssen et al. 2019a; Lahén et al. 2019; Ma et al. 2020).

We also find there can be significant overlaps in orbital properties between *in situ* and accreted GCs. Though the *in situ* GCs are generally biased to low energies (small apocentres), they exhibit a large tail to high energies and even retrograde orbits (relative to the present-day disc), such that there is a significant overlap between *in situ* and accreted GCs. The high-energy *in situ* GCs are generally old and metal poor, meaning it may not be possible to unambiguously distinguish between *in situ* and accreted GCs in these cases.

We find that the orbits of GC subpopulations may hold particular power in recovering the properties of their progenitor galaxy, though there exists a degeneracy between the galaxy mass and the accretion redshift when considering only orbital properties. In this paper we rely on existing estimates for galaxy masses to derive merger redshifts, breaking this degeneracy therefore requires combining the orbital properties with other tracers. We undertake this in a companion paper (Kruijssen et al. 2020), combining the GC subpopulation orbits with their ages and metallicities to recover their progenitor galaxy properties using information about the GC sub-systems alone. All of our estimated accretion redshifts in this paper are consistent to within the formal uncertainties with the predictions of Kruijssen et al. (2020); however, the extra age and metallicity information used in that paper allows us to simultaneously derive progenitor galaxy masses. The combination of age–metallicity information with orbital properties therefore greatly increases the power of GCs in their use as tracers of galaxy formation and assembly.

ACKNOWLEDGEMENTS

We thank the referee for a helpful and constructive report. JLP and NB gratefully acknowledge funding from a European Research Council consolidator grant (ERC-CoG-646928-Multi-Pop). JMDK gratefully acknowledges funding from the Deutsche Forschungsgemeinschaft (DFG, German Research Foundation) through an Emmy Noether Research Group (grant number KR4801/1-1). JMDK, STG, and MRC gratefully acknowledge funding from the European Research Council (ERC) under the European Union's Horizon 2020 research and innovation programme via the ERC Starting Grant MUSTANG (grant agreement number 714907). MRC is supported by a Fellowship from the International Max Planck Research School for Astronomy and Cosmic Physics at the University of Heidelberg (IMPRS-HD). NB and RAC are Royal Society University Research Fellows. This work used the DiRAC Data Centric system at Durham University, operated by the Institute for Computational Cosmology on behalf of the STFC DiRAC HPC Facility (www.dirac.ac.uk). This equipment was funded by BIS National E-infrastructure capital grant ST/K00042X/1, STFC capital grants ST/H008519/1 and ST/K00087X/1, STFC DiRAC Operations grant ST/K003267/1, and Durham University. DiRAC is part of the National E-Infrastructure. The work also made use of high performance

computing facilities at Liverpool John Moores University, partly funded by the Royal Society and LJMU's Faculty of Engineering and Technology.

DATA AVAILABILITY

The data underlying this article will be shared on reasonable request to the corresponding author.

REFERENCES

Abadi M. G., Navarro J. F., Steinmetz M., Eke V. R., 2003, ApJ, 597, 21
Adamo A., Bastian N., 2018, in Stahler S., ed., Astrophysics and Space Science Library, Vol. 424, The Birth of Star Clusters. Springer, Berlin, p. 91
Bahé Y. M. et al., 2016, MNRAS, 456, 1115
Baumgardt H., Hilker M., Sollima A., Bellini A., 2019, MNRAS, 482, 5138
Bellazzini M., Correnti M., Ferraro F. R., Monaco L., Montegriffo P., 2006, A&A, 446, L1
Belokurov V., Erkal D., Evans N. W., Koposov S. E., Deason A. J., 2018, MNRAS, 478, 611
Belokurov V., Sanders J. L., Fattahi A., Smith M. C., Deason A. J., Evans N. W., Grand R. J. J., 2020, MNRAS, 494, 3880
Bignone L. A., Helmi A., Tissera P. B., 2019, ApJ, 883, L5
Binney J., Tremaine S., 2008, Galactic Dynamics, 2nd edn. Princeton Univ. Press, Princeton
Blumenthal G. R., Faber S. M., Primack J. R., Rees M. J., 1984, Nature, 311, 517
Brodie J. P., Strader J., 2006, ARA&A, 44, 193
Brown J. A., Wallerstein G., Zucker D., 1997, AJ, 114, 180
Burkert A., Truran J. W., Hensler G., 1992, ApJ, 391, 651
Carollo D. et al., 2007, Nature, 450, 1020
Chandrasekhar S., 1943, ApJ, 97, 255
Chiba M., Beers T. C., 2000, AJ, 119, 2843
Conroy C., Gunn J. E., 2010, ApJ, 712, 833
Conroy C., Gunn J. E., White M., 2009, ApJ, 699, 486
Conroy C., Naidu R. P., Zaritsky D., Bonaca A., Cargile P., Johnson B. D., Caldwell N., 2019, ApJ, 887, 237
Correa C. A., Schaye J., Clauwens B., Bower R. G., Crain R. A., Schaller M., Theuns T., Thob A. C. R., 2017, MNRAS, 472, L45
Crain R. A. et al., 2015, MNRAS, 450, 1937
Crain R. A. et al., 2017, MNRAS, 464, 4204
Deason A. J., Belokurov V., Koposov S. E., Lancaster L., 2018, ApJ, 862, L1
Deason A. J., Belokurov V., Sanders J. L., 2019, MNRAS, 490, 3426
Di Matteo P., Fragkoudi F., Khoperskov S., Ciambur B., Haywood M., Combes F., Gómez A., 2019, A&A, 628, A11
Dinescu D. I., Girard T. M., van Altena W. F., 1999, AJ, 117, 1792
Dolag K., Borgani S., Murante G., Springel V., 2009, MNRAS, 399, 497
Dotter A. et al., 2010, ApJ, 708, 698
Dotter A., Sarajedini A., Anderson J., 2011, ApJ, 738, 74
Dubinski J., 1994, ApJ, 431, 617
Eggen O. J., Lynden-Bell D., Sandage A. R., 1962, ApJ, 136, 748
Elmegreen B. G., Efremov Y. N., 1997, ApJ, 480, 235
Forbes D. A., 2020, MNRAS, 493, 847
Forbes D. A., Bridges T., 2010, MNRAS, 404, 1203
Forbes D. A. et al., 2018, Proc. R. Soc. A, 474, 20170616
Freeman K., Bland-Hawthorn J., 2002, ARA&A, 40, 487
Furlong M. et al., 2015, MNRAS, 450, 4486
Furlong M. et al., 2017, MNRAS, 465, 722
Gaia Collaboration, 2016, A&A, 595, A2
Gaia Collaboration, 2018, A&A, 616, A1
Hammer F., Puech M., Chemin L., Flores H., Lehnert M. D., 2007, ApJ, 662, 322
Hashimoto Y., Funato Y., Makino J., 2003, ApJ, 582, 196
Haywood M., Di Matteo P., Lehnert M. D., Snaith O., Khoperskov S., Gómez A., 2018, ApJ, 863, 113
Helmi A., 2008, A&AR, 15, 145
Helmi A., White S. D. M., de Zeeuw P. T., Zhao H., 1999, Nature, 402, 53
Helmi A., Babusiaux C., Koppelman H. H., Massari D., Veljanoski J., Brown A. G. A., 2018, Nature, 563, 85
Horta D. et al., 2020, MNRAS, 493, 3363
Hughes M. E., Pfeffer J., Martig M., Bastian N., Crain R. A., Kruijssen J. M. D., Reina-Campos M., 2019, MNRAS, 482, 2795
Hughes M. E., Pfeffer J. L., Martig M., Reina-Campos M., Bastian N., Crain R. A., Kruijssen J. M. D., 2020, MNRAS, 491, 4012
Ibata R. A., Gilmore G., Irwin M. J., 1994, Nature, 370, 194
Ibata R. A., Wyse R. F. G., Gilmore G., Irwin M. J., Suntzeff N. B., 1997, AJ, 113, 634
Iorio G., Belokurov V., 2019, MNRAS, 482, 3868
Irrgang A., Wilcox B., Tucker E., Schiefelbein L., 2013, A&A, 549, A137
Kazantzidis S., Kravtsov A. V., Zentner A. R., Allgood B., Nagai D., Moore B., 2004, ApJ, 611, L73
Keller B. W., Kruijssen J. M. D., Pfeffer J., Reina-Campos M., Bastian N., Trujillo-Gomez S., Hughes M. E., Crain R. A., 2020, MNRAS, 495, 4248
Kepley A. A. et al., 2007, AJ, 134, 1579
Koch A., Côté P., 2019, A&A, 632, A55
Koppelman H. H., Helmi A., Massari D., Roelenga S., Bastian U., 2019a, A&A, 625, A5
Koppelman H. H., Helmi A., Massari D., Price-Whelan A. M., Starkenburg T. K., 2019b, A&A, 631, L9
Kravtsov A. V., Gnedin O. Y., 2005, ApJ, 623, 650
Kruijssen J. M. D., 2012, MNRAS, 426, 3008
Kruijssen J. M. D., 2014, Class. Quantum Gravity, 31, 244006
Kruijssen J. M. D., 2015, MNRAS, 454, 1658
Kruijssen J. M. D., Pelupessy F. I., Lamers H. J. G. L. M., Portegies Zwart S. F., Icke V., 2011, MNRAS, 414, 1339
Kruijssen J. M. D., Pfeffer J. L., Crain R. A., Bastian N., 2019a, MNRAS, 486, 3134
Kruijssen J. M. D., Pfeffer J. L., Reina-Campos M., Crain R. A., Bastian N., 2019b, MNRAS, 486, 3180
Kruijssen J. M. D. et al., 2020, MNRAS, 498, 2472
Lagos C. d. P. et al., 2015, MNRAS, 452, 3815
Lagos C. d. P. et al., 2016, MNRAS, 459, 2632
Lahén N., Naab T., Johansson P. H., Elmegreen B., Hu C.-Y., Walch S., 2019, ApJ, 879, L18
Larson R. B., 1976, MNRAS, 176, 31
Leaman R., VandenBerg D. A., Mendel J. T., 2013, MNRAS, 436, 122
Li H., Gnedin O. Y., Gnedin N. Y., Meng X., Semenov V. A., Kravtsov A. V., 2017, ApJ, 834, 69
Lin D. N. C., Richer H. B., 1992, ApJ, 388, L57
Ma X. et al., 2020, MNRAS, 493, 4315
Mackereth J. T., Crain R. A., Schiavon R. P., Schaye J., Theuns T., Schaller M., 2018, MNRAS, 477, 5072
Mackereth J. T. et al., 2019, MNRAS, 482, 3426
Mackey A. D., Gilmore G. F., 2004, MNRAS, 355, 504
Mackey A. D., van den Bergh S., 2005, MNRAS, 360, 631
McMillan P. J., 2017, MNRAS, 465, 76
Majewski S. R., 1993, ARA&A, 31, 575
Marasco A., Crain R. A., Schaye J., Bahé Y. M., van der Hulst T., Theuns T., Bower R. G., 2016, MNRAS, 461, 2630
Marín-Franch A. et al., 2009, ApJ, 694, 1498
Massari D., Koppelman H. H., Helmi A., 2019, A&A, 630, L4
Matteucci F., Francois P., 1989, MNRAS, 239, 885
Muñoz-Mateos J. C., Gil de Paz A., Boissier S., Zamorano J., Jarrett T., Gallego J., Madore B. F., 2007, ApJ, 658, 1006
Myeong G. C., Evans N. W., Belokurov V., Amorisco N. C., Koposov S. E., 2018a, MNRAS, 475, 1537
Myeong G. C., Evans N. W., Belokurov V., Sanders J. L., Koposov S. E., 2018b, MNRAS, 478, 5449
Myeong G. C., Evans N. W., Belokurov V., Sanders J. L., Koposov S. E., 2018c, ApJ, 856, L26
Myeong G. C., Evans N. W., Belokurov V., Sanders J. L., Koposov S. E., 2018d, ApJ, 863, L28

Myeong G. C., Vasiliev E., Iorio G., Evans N. W., Belokurov V., 2019, MNRAS, 488, 1235
Necib L., Ostdiek B., Lisanti M., Cohen T., Freytsis M., Garrison-Kimmel S., 2019, preprint (arXiv:1907.07681)
Necib L. et al., 2020, Nat. Astron., in press
Niederste-Ostholt M., Belokurov V., Evans N. W., Peñarrubia J., 2010, ApJ, 712, 516
Pfeffer J., Kruijssen J. M. D., Crain R. A., Bastian N., 2018, MNRAS, 475, 4309
Pfeffer J., Bastian N., Crain R. A., Kruijssen J. M. D., Hughes M. E., Reina-Campos M., 2019a, MNRAS, 487, 4550
Pfeffer J., Bastian N., Kruijssen J. M. D., Reina-Campos M., Crain R. A., Usher C., 2019b, MNRAS, 490, 1714
Planck Collaboration I, 2014, A&A, 571, A1
Portegies Zwart S. F., McMillan S. L. W., Gieles M., 2010, ARA&A, 48, 431
Pritzl B. J., Venn K. A., Irwin M., 2005, AJ, 130, 2140
Reina-Campos M., Kruijssen J. M. D., 2017, MNRAS, 469, 1282
Reina-Campos M., Kruijssen J. M. D., Pfeffer J., Bastian N., Crain R. A., 2018, MNRAS, 481, 2851
Reina-Campos M., Kruijssen J. M. D., Pfeffer J. L., Bastian N., Crain R. A., 2019, MNRAS, 486, 5838
Sales L. V., Navarro J. F., Theuns T., Schaye J., White S. D. M., Frenk C. S., Crain R. A., Dalla Vecchia C., 2012, MNRAS, 423, 1544
Sanderson R. E. et al., 2018, ApJ, 869, 12
Schaye J. et al., 2015, MNRAS, 446, 521
Searle L., Zinn R., 1978, ApJ, 225, 357
Springel V., White S. D. M., Tormen G., Kauffmann G., 2001, MNRAS, 328, 726
Springel V., White S. D. M., Hernquist L., 2004, in Ryder S., Pisano D., Walker M., Freeman K., eds, Proc. IAU Symp. 220, Dark Matter in Galaxies. Kluwer, Dordrecht, p. 421
Stewart K. R., Bullock J. S., Wechsler R. H., Maller A. H., Zentner A. R., 2008, ApJ, 683, 597
Thob A. C. R. et al., 2019, MNRAS, 485, 972
Trayford J. W. et al., 2015, MNRAS, 452, 2879
Trujillo-Gomez S., Kruijssen J. M. D., Reina-Campos M., Pfeffer J. L., Keller B. W., Crain R. A., Bastian N., Hughes M. E., 2020, preprint (arXiv:2005.02401)
Usher C., Pfeffer J., Bastian N., Kruijssen J. M. D., Crain R. A., Reina-Campos M., 2018, MNRAS, 480, 3279
VandenBerg D. A., Brogaard K., Leaman R., Casagrande L., 2013, ApJ, 775, 134
van den Bergh S., 1993, ApJ, 411, 178
van den Bosch F. C., Lewis G. F., Lake G., Stadel J., 1999, ApJ, 515, 50
Vasiliev E., 2019, MNRAS, 484, 2832
Velazquez H., White S. D. M., 1995, MNRAS, 275, L23
White S. D. M., Rees M. J., 1978, MNRAS, 183, 341
Wyse R. F. G., 2001, in Funes J. G., Corsini E. M., eds, ASP Conf. Ser. Vol. 230, Galaxy Disks and Disk Galaxies. Astron. Soc. Pac., San Francisco, p. 71
Zinn R., 1993, in Smith G. H., Brodie J. P., eds, ASP Conf. Ser. Vol. 48, The Globular Cluster-Galaxy Connection. Astron. Soc. Pac., San Francisco, p. 38

This paper has been typeset from a TEX/LATEX file prepared by the author.